Extreme Double/Triple Asymmetric Epitaxial Structure Based Diode Lasers for High Powers and High Efficiencies

Xiaolei Zhao, Siwei Zeng, Lance Sweat, and Lin Zhu, *Member, IEEE*

***Abstract*—In edge-emitting high power laser diodes, the longitudinal spatial hole burning (LSHB) effect induced by the inhomogeneous photon and carrier distributions and the non-linear process, two-photon absorption (TPA), are demonstrated to the key causes of power saturation at the high injection level even in the absence of thermal roll-over. Laser diodes based on extreme, double/triple asymmetric (EDAS/ETAS) epitaxial structures show great potentials in high-power and high-efficiency applications owing to the reduced series resistance, low optical loss, and suppressed power saturation. In this paper, a novel semi-analytical calculation method is proposed to systematically analyze the impact of LSHB and TPA effects on the output characteristics of EDAS/ETAS-based broad area lasers (BALs). By leveraging the feature that it is flexible to adjust the confinement factor of ETAS epitaxial structure without compromising the internal loss and resistance level, the laser parameters are first optimized to minimize power saturation of ETAS-based BALs under pulsed and Continuous Wave (CW) operation.**

***Index Terms*—Semiconductor lasers, quantum well lasers, semiconductor device modeling, power conversion.**

I. Introduction

HIGH-POWER broad-area laser (BAL) diodes are key components in numerous modern technologies, such as pump sources for solid state or fiber laser systems, laser radar, medical apparatus, and material processing [1]–[4]. They are also important for developing high-performance single-mode laser diodes for high brightness applications. In all these applications, there is a continuing demand for the increased achievable output power with a high electro-optical power conversion efficiency (PCE). Over the past decades, many advanced epitaxial designs have been developed, among which the Extreme, double/triple asymmetric (EDAS/ETAS) structures with very thin p-waveguide design show distinct advantages in improving PCE owing to reduced series resistance, low optical loss, and suppressed power saturation [5]–[12]. An EDAS-based BAL with a 100 μm stripe width and 4 mm cavity length was reported to reach a power conversion efficiency of 60% at 12W CW power under room temperature conditions [8]. An ETAS-based 100 μm-width BAL with optimized confinement factor delivered an efficiency of 63% at 14 W [9]. It was also recently reported that very high efficiency $> 70\%$ was achieved from the 4 mm-long 186um-wide ETAS based BAL by balancing the confinement factor and front facet reflectivity [10]. Further increase of the output power and efficiency is challenging. For high-power laser diodes, their front and rear facets are commonly coated with highly asymmetric reflective films to improve the slope efficiency and extract most of optical powers from the front facet. Additionally, long cavities are employed to lower the thermal resistance for better thermal management and higher reliability. However, these two design features result in an inhomogeneous distribution of photon and free carrier densities and thus non-uniform optical gain profile along the laser longitudinal direction, leading to the so-called longitudinal spatial hole burning (LSHB) effect [13]–[17] and a reduction in laser output power. Moreover, two-photon absorption (TPA), a nonlinear process in semiconductors, is also considered to be one of the fundamental factors limiting the maximum achievable optical power in high-power laser diodes [18]–[20].

In this work, a semi-analytical calculation model that incorporates LSHB and TPA effects is used to gain an in-depth understanding of how laser design parameters affect the output power and the conversion efficiency, thereby achieving design optimization of EDAS/ETAS-based diode lasers. To make the model better reflect the real situation, the commercial software LASTIP is used to provide the basic L-I and V-I curves of the designed BAL devices without considering LSHB and TPA effects first. LASTIP is a two-dimensional (2D) simulator for edge-emitting Fabry-Perot laser diodes, which can self-consistently combines multi-mode wave guiding, carrier transport, quantum well optical gain, and heat flow in the transverse plane [21]. In what follows, we begin by extracting the key parameters, such as the internal quantum efficiency, the carrier density dependent material gain curve, the confinement factor, and current-dependent internal loss of the representative EDAS and ETAS-based BAL devices from LASTIP and discuss their advantages for high-power operation over the BAL device based on a conventional epitaxial structure. In Section III, models for the direct and indirect TPA effects are discussed in detail and

Manuscript received April 20, 2022; accepted May 17, 2022. Date of publication May 23, 2022; date of current version June 8, 2022. This work was supported in part by Army Research Office under Grant W911NF-18-1-0176 and in part by the Office of Naval Research under Grant N00014-17-1-2556. *(Corresponding author: Xiaolei Zhao.)*

The authors are with the Department of Electrical and Computer Engineering and Center for Optical Materials Science and Engineering Technologies, Clemson University, Clemson, SC 29634 USA (e-mail: xiaolei@g.clemson.edu; szeng@g.clemson.edu; lsweatt@g.clemson.edu; zhu3@clemson.edu).

Digital Object Identifier 10.1109/JPHOT.2022.3176811

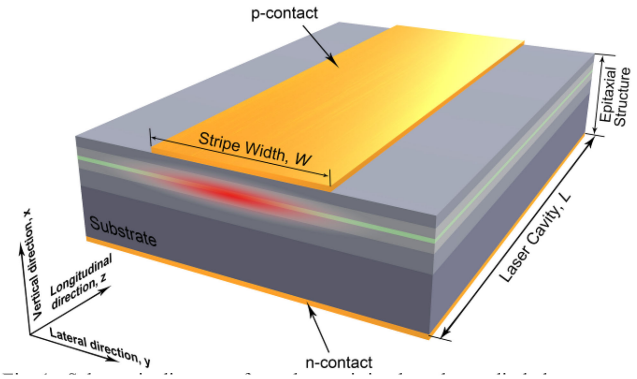

Fig. 1. Schematic diagram of an edge-emitting broad area diode laser.

then the modified rate equation incorporating the LSHB and TPA effects is introduced. Following this modified rate equation, we explore how various laser design parameters impact on the output power and conversion efficiency of EDAS/ETAS-based BALs. By utilizing the feature that ETAS epitaxial structure is flexible in controlling the confinement factor, we perform design optimization procedures for the ETAS-based BAL under pulsed and Continuous Wave (CW) high-power operation in Sections IV and V. Our work provides a promising semi-analytical method for obtaining high-power and high-efficiency ETAS-based BALs, which is much more efficient and time-saving compared with a full 3D simulation model.

II. Analysis Based on Standard Rate Equations

Fig. 1 shows the schematic of an edge-emitting BAL with the coordinate system used in this paper. The behaviors of diode lasers are commonly established by a phenomenological approach through a set of coupled rate equations related to photon density, carrier density, and optical gain. The standard one-dimensional (1D) rate equation set generally assumes uniform longitudinal distributions of carrier and photon densities within the laser cavity and can be written as [22]

$$\frac{dN}{dt} = \frac{\eta_i I}{qV} - \frac{N}{\tau(N)} - v_g g(N) N_p \tag{1a}$$

$$\frac{dN_p}{dt} = \Gamma v_g g(N) N_p - \frac{N_p}{\tau_p(I)} \tag{1b}$$

Here, N and N_p respectively represent the carrier and photon densities in the active region. I is defined as the injection current, q as the electron charge, η_i as the internal quantum efficiency, v_g as the photon group velocity and $V = dWL$ as the active region volume with d, W, and L respectively being the active layer thickness, stripe width, and cavity length. η_i is taken as 0.97, which is extracted from LASTIP by dividing the integral of the total recombination rate in the active region underneath the p contact by the injection current. $(N) = 1/(A+BN+CN^2)$ is the carrier lifetime, where the three terms respectively characterize the Shockley-Read-Hall, spontaneous radiation, and Auger recombination contributions. The coefficients of Shockley-Read-Hall $A = 7.1 \times 10^8$ s^{-1}, spontaneous radiation $B = 1 \times 10^{-10}$ cm^{3}s^{-1}, and Auger recombination $C_n = C_p = 2 \times 10^{-30}$ cm^{6}s^{-1} are taken from literature [6]. $g(N)$ stands for the carrier density dependent material gain. In (1b), Γ is the confinement factor and $\tau_p(I)$ is the photon lifetime. $\tau_p(I)$ can be calculated by use of the relation $1/\tau_p(I) = v_g[\alpha_i(I) + \alpha_m]$, where $\alpha_m = -1/(2L)\ln(R_f R_r)$ is the mirror loss with R_f and R_r being the front and rear facet reflectivity, respectively. $\alpha_i(I)$ represents the current-dependent internal optical loss, which mainly comes from the scattering and free carrier induced absorption. The scattering loss is assumed to be constant. But the free carrier absorption (FCA) generally increases with the injection current because the carrier density does not pin at threshold but increases with the injection current, *i.e.,* the carrier non-pinning effect [23], [24].

For the steady state, i.e., $dN_p/dt = 0$ and $dN/dt = 0$, we can find the values of $N_{th}(I)$ by solving equation $\Gamma g(N_{th}) = \alpha_i(I) + \alpha_m$. Then the threshold current $I_{th}(I)$ can be further obtained by applying $N_p = 0$ into (1a). The idealized output power-current (L-I) curves without the LSHB and TPA effects can be calculated from

$$P_{out}(I > I_{th}) = \frac{\hbar\omega}{q}\eta_i\eta_d(I)[I - I_{th}(I)] \tag{2}$$

where $\eta_d(I) = \alpha_m/[\alpha_i(I) + \alpha_m]$ is defined as the differential quantum efficiency (DQE). In order to allow the above rate equations to better predict the power output characteristics of BAL diodes based on different epitaxial structures, here we employ the simulation software LASTIP to provide the required parameter values such as the internal quantum efficiency η_i, the carrier density dependent material gain curve $g(N)$, the confinement factor Γ, and current-dependent internal loss $\alpha_i(I)$ Additionally, LASTIP is used to provide the electric characteristics of laser devices for analyzing their conversion efficiencies. Next, we explore the output characteristics of three representative epitaxial structure designs (conventional, EDAS, and ETAS) when LSHB and TPA effects are not considered.

The refractive index and the fundamental vertical mode intensity profiles for the three epitaxial designs are plotted in Fig. 2(a)–(c), respectively. The three epitaxial structures use the same active region designs of a compressively strained InGaAs single quantum well (thickness $d = 8$ nm) and GaAsP barriers with the emitting wavelength around 940 nm. Their main difference lies in the AlGaAs waveguide structure. As for the conventional design, the active region is placed in a symmetric waveguide structure with the waveguide core thickness of 800 nm. The EDAS design has a very asymmetric waveguide structure with thick graded index (GRIN) n-waveguide layers, very thin GRIN p-waveguide layers and a large index step at the waveguide-cladding interface on the p-side. The resulting fundamental mode shifts to the n-side and thus has only a small overlap with the p doped region, leading to much less optical free carrier absorption loss. The thin p-layers also ensure lower series resistance and carrier leakage. On the other hand, the EDAS structure is generally inherited with a small optical confinement factor and thus low modal gain. In the EDAS design, as shown in the inset of Fig. 2(b), the thicknesses of the n- and p-GRIN waveguide layers closest to the active region (in the following we refer to them as the confinement layers) are equal, that is, $t_n = t_p$. Different from EDAS, the ETAS design adopts

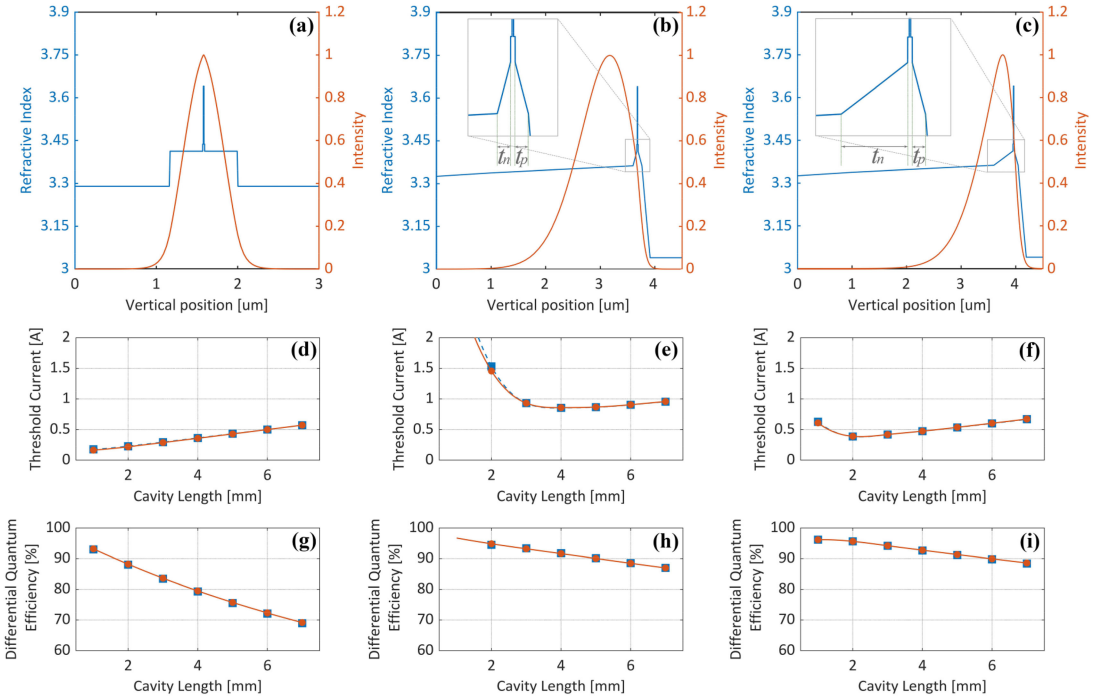

Fig. 2. Refractive index (Blue, left axis) and fundamental vertical mode intensity (Red, right axis) profiles for (a) a conventional epitaxial structure, (b) an EDAS ($t_n = t_p = 70$ nm) and (c) an ETAS ($t_n = 350$ nm, $t_p = 70$ nm) epitaxial design. Calculated threshold current (d-f) and differential quantum efficiency (g-i) of broad area lasers based on the three designs as a function of laser cavity length (stripe width $W = 100$ μm, reflectivities of the front and rear facet $R_f = 1\%$ and $R_r = 98\%$). Blue rectangle and red circle symbols are respectively the simulation results from LASTIP and the calculation results by solving (1). Dashed and solid curves are the corresponding spherical linear interpolations.

an additional (third) asymmetry ($t_n \neq t_p$) in the waveguide structure, as illustrated by Fig. 2(c), providing a new degree of freedom to tailor the optical modal shape and optimize device performances. For example, by adjusting the size of t_n with other structural parameters unchanged, we can flexibly control the confinement factor to vary in a relatively large range while not introducing excessive light intensity in the p-doped region, thereby maintaining the low optical loss level.

LASTIP simulations for BALs based on the above three epitaxial designs are performed first. In this study, we assume the p-side contact width to be $W = 100$ μm. Full 2D simulations are conducted to better reveal the current spreading and multi-lateral mode behavior in BALs. The vertical optical mode is calculated by solving the vertical Helmholtz wave equation. The effective index method is used to treat the multi-lateral modes with ten transverse standing waves considered. The reflectivities of the front and rear facets are respectively fixed as $R_f = 1\%$ and $R_r = 98\%$. The extracted threshold currents of the three BAL designs as a function of laser cavity length are plotted as the blue rectangles in Fig. 2(d)–(f). As expected, the threshold currents of the conventional design are smallest among the three designs since it has the largest confinement factor. It can also be found that its threshold current gradually increases as the cavity length L increases. Although the reduction in mirror loss will result in a lower threshold current density J_{th} for a longer cavity length, the increase in the contact area eventually causes the threshold current I_{th} to increase with the increase of cavity length. EDAS design has the largest threshold current on account of its smallest confinement factor. In addition, for the short cavity lengths, i.e., when the mirror loss is relatively high, the small modal gain in EDAS makes it more difficult to reach the threshold condition. Therefore, the threshold current of the EDAS-based BAL increases sharply when the cavity length L is smaller than 3 mm. For the ETAS design, the third asymmetry helps to increase its confinement factor and thus threshold currents are effectively reduced. Fig. 2(g)–(i) show the simulated DQE of the three BAL designs versus cavity length at the injection current $I = \sim 3$ A. Owing to the relatively high internal loss, the DQE of the conventional BAL design drops significantly as the cavity length increases, which indicates that this design needs further improvement for high power operation. The low internal loss level in the EDAS and ETAS-based BALs enables them to maintain a high DQE even with a long cavity length, so they have great potential for high power applications. The red circles in Fig. 2(d)–(i) are the calculation results by solving rate equation (1) with the extracted parameters from LASTIP. It can be seen that, except for the slight deviations of the threshold current values in the case of short cavity, the calculation results are almost same with the simulation results of LASTIP, proving that the 1D rate equations can be used to well predict the power output characteristics of BAL diodes based on different epitaxial structures.

III. Equations With LSHB and TPA Effects

For high-power diode lasers, the carrier and photon inhomogeneity along the longitudinal direction significantly affects the laser characteristics especially at high injection currents, which

is not considered in the standard rate equation set (1). In addition, given the high optical light intensities in high-power diode lasers, the nonlinear optical losses caused by TPA effect become important and non-negligible under high injection levels. More specifically, the TPA effect involves, in fact, two mechanisms contributing to the nonlinear optical losses [20]: (i) the direct effect of nonlinear loss due to TPA, and (ii) the indirect effect of the TPA serving as another source of carrier accumulation in semiconductor lasers, creating additional optical losses through free carrier induced absorption.

The direct TPA loss at any local point in the laser cavity can be given as [20]

$$\alpha_{TPA}^{\text{direct}}(x,z) = \beta(x)\,\Psi(x,z) \tag{3}$$

where $\beta(x)$ [cm/GW] denotes the TPA coefficient. β is material composition dependent, so here it shows a dependence on the vertical coordinate x. For the specific calculation method of β, please refer to Ref [18]. $\Psi(x, z)$ represents the local light intensity. If it is assumed that the optical power is uniformly distributed in the lateral direction, then $J(x, z)$ can be written as $\Psi(x,z) = P(z)\varphi^2(x)/W$, where $P(z)$ is the local power and $\varphi^2(x)$ is the normalized optical mode intensity profile, i.e., $\int_{-\infty}^{+\infty}\varphi^2(x)\mathrm{d}x = 1$. The modal loss caused by the direct TPA effect can be calculated as

$$\begin{aligned}\alpha_{TPA}^{\text{direct,modal}}(z) &\approx \int_{-\infty}^{+\infty}\alpha_{TPA}^{\text{direct}}(x,z)\,\varphi^2(x)\mathrm{d}x \\ &\approx \frac{P(z)}{W}\int_{-\infty}^{+\infty}\beta(x)\,\varphi^4(x)\mathrm{d}x\end{aligned} \tag{4}$$

The local power $P(z)$ can be expressed by the average photon density in the active region. That is,

$$P(z) = \frac{dW}{\Gamma}\left[v_g\hbar\omega N_p(z)\right] \tag{5}$$

After substituting (5) into (4), we obtain that

$$\begin{aligned}\alpha_{TPA}^{\text{direct,modal}} &\approx \frac{d}{\Gamma}v_g\hbar\omega N_p(z)\int_{-\infty}^{+\infty}\beta(x)\,\varphi^4(x)\mathrm{d}x \\ &\approx \beta_{TPA}^{\text{direct,modal}}N_p(z)\end{aligned} \tag{6}$$

with $\beta_{TPA}^{\text{direct,modal}} = \frac{d}{\Gamma}v_g\hbar\omega\int_{-\infty}^{+\infty}\beta(x)\varphi^4(x)\mathrm{d}x$ defined as the direct modal TPA coefficient. Fig. 3 plots the dependance of the calculated direct modal TPA coefficient $\beta_{TPA}^{\text{direct,modal}}$ (blue, left axis) and the confinement factor Γ (red, right axis) of the ETAS epitaxy on the *n*-confinement layer thickness t_n. The confinement factor Γ increases monotonically with t_n. But its growth rate gradually slows down for relatively large values of t_n, indicating that Γ is close to its maximum achievable value. Continuing to increase Γ requires additional adjustments to the epitaxial layer composition. The calculated direct modal TPA coefficient $\beta_{TPA}^{\text{direct,modal}}$ shows a strong dependance on the epitaxial structure. As t_n increases, $\beta_{TPA}^{\text{direct,modal}}$ initially declines rapidly, reaching a minimum at $t_n = 280$ nm and increasing slightly thereafter.

As for the indirect TPA effect, its contribution to the optical internal loss is determined by the TPA-generated free electron density $\Delta N_{e,TPA}$ and hole density $\Delta N_{h,TPA}$. That is,

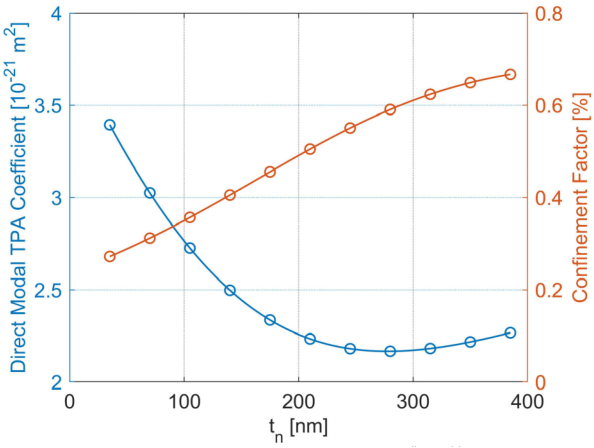

Fig. 3 The calculated direct modal TPA coefficient βdirect,modal TPA(blue, left axis) and confinement factor Γ (red, right axis) of the ETAS epitaxy as function of the n-confinement layer thickness t_n.

$$\begin{aligned}\alpha_{TPA}^{\text{indirect,modal}}(z) \approx\ & \sigma_e\int_{-\infty}^{+\infty}\Delta N_{e,TPA}(x,z)\,\varphi^2(x)\mathrm{d}x \\ &+ \sigma_h\int_{-\infty}^{+\infty}\Delta N_{h,TPA}(x,z)\,\varphi^2(x)\mathrm{d}x\end{aligned} \tag{7}$$

where σ_e and σ_h are respectively the free-electron and free-hole absorption cross-sections. To obtain $\Delta N_{e,TPA}$ and $\Delta N_{h,TPA}$, we should solve the carrier transport equation of the full drift-diffusion model with the TPA generation term given by the TPA rate [20]:

$$G(x,z) \approx \frac{\beta(x)}{\hbar\omega}\left[\frac{P(z)^2}{W}\right]\varphi^4(x) \tag{8}$$

The new version of LASTIP follows this model and automatically includes the TPA-generated free carrier density in its calculations if the TPA coefficient is properly defined. The definition of TPA coefficient in LASTIP is same as (6) [21]. Therefore, in this work we use LASTIP to calculate the TPA-generated free carrier density distribution $\Delta N_{e,TPA}(x)$ and $\Delta N_{h,TPA}(x)$. Note that the longitudinal direction z dependance of $\Delta N_{e,TPA}$ and $\Delta N_{h,TPA}$ is ignored as LASTIP is a 2D simulator. Fig. 4(a) shows the calculated TPA-generated free carrier density distribution of 4 mm-long ETAS BALs at injection current $I =$ 40 A. It can be observed that the TPA-generated free electrons and holes both mainly concentrate in the active region and the n-side cladding layer (especially around the interface where high doping begins). Using the data of $\Delta N_{e,TPA}(x)$ and $\Delta N_{h,TPA}(x)$, we can obtain the indirect TPA modal absorption by (7). Fig. 4(b) and (c) respectively show the dependance of the calculated indirect TPA absorptions $\alpha_{TPA}^{\text{indirect,modal}}$ of 4 mm-long ETAS-based BALs on the injection current I and the *n*-confinement layer thickness t_n. As expected, $\alpha_{TPA}^{\text{indirect,modal}}$ increases with the injection current owing to the square term of power in the indirect TPA generation rate. The dependance of the indirect TPA absorption $\alpha_{TPA}^{\text{indirect,modal}}$ on t_n is similar to that of the

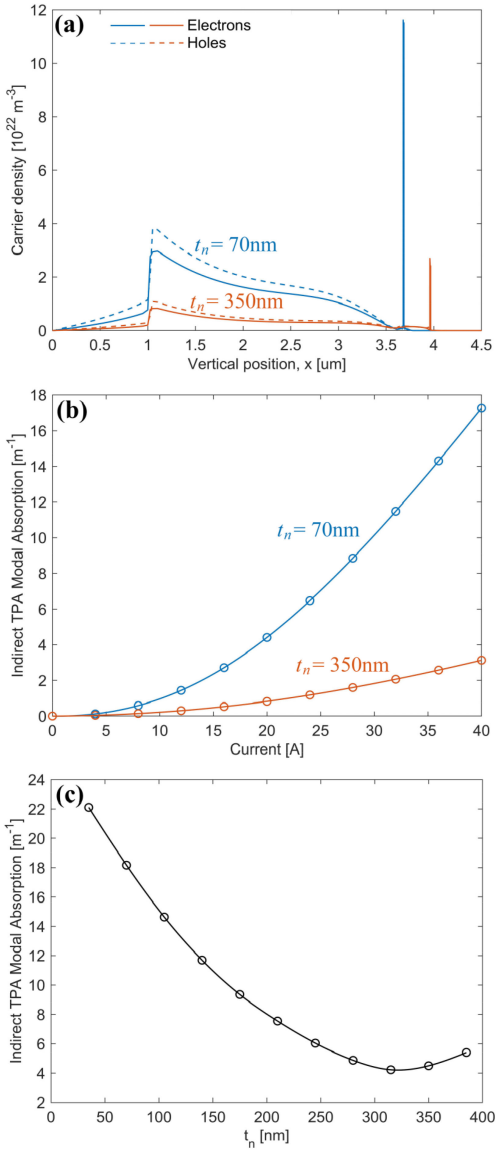

Fig. 4 Calculated spatial distributions of TPA-generated free carrier densities at $I = 40$ A (a), and dependance of indirect TPA absorption on injection current (b) for 4 mm-long ETAS BALs. Blue: $t_n = 70$ nm; and red: $t_n = 350$ nm. (c) Calculated indirect TPA absorption as a function of the *n*-confinement layer thickness t_n at $I = 40$ A.

direct one $\alpha_{TPA}^{\text{direct,modal}}$. The difference is that the position of the minimum of $\alpha_{TPA}^{\text{indirect,modal}}$ shifts towards a larger t_n value of ~315 nm.

Taking into account the LSHB and TPA effects discussed above, the steady state 1D rate equations are modified as

$$\frac{\eta_i I}{qV} - \frac{N(z)}{\tau[N(z)]} - v_g g[N(z)]\left[N_p^+(z) + N_p^-(z)\right] = 0 \quad (9a)$$

$$\frac{dN_p^{\pm}(z)}{dz} = \pm\left\{\begin{array}{l}\Gamma v_g g[N(z)] N_p^{\pm}(z) - \\ \left[\alpha_i(I) + \alpha_{TPA}^{\text{indirect,modal}}(I)\right] N_p^{\pm}(z) \\ -\beta_{TPA}^{\text{direct,modal}} N_p^{\pm}(z)^2\end{array}\right\} \quad (9b)$$

where z stands for the longitudinal axis position, $N(z)$ is the local carrier density, $N_P^+(z)$ and $N_P^-(z)$ are forward and reverse propagating photon densities, respectively. Instead of the average mirror loss in the standard rate equation, the forward and reverse propagating photon densities in the modified equations should satisfy the boundary conditions at the front facet ($z = 0$) and the rear facet ($z = L$) to accommodate their spatial non-uniformity:

$$N_p^+(0) = R_f N_p^-(0) \quad (11a)$$

$$N_p^-(L) = R_r N_p^+(L) \quad (11b)$$

By solving the coupled differential equations with the boundary conditions, the output power is then determined as

$$P_{out} = v_g W \frac{d}{\Gamma} \hbar\omega \left[N_p^-(0)(1 - R_f) + N_p^+(L)(1 - R_r)\right] \quad (12)$$

IV. Design Optimization for Pulsed Operation

Based on the rate equations with LSHB and TPA effects discussed in the previous section, we will investigate how the laser structural parameters of the ETAS-based BAL impact its output power and efficiency. In this section, we do not consider the impact of thermal effects, which effectively corresponds to pulsed (quasi-CW) operation regime. The calculated *L-I* characteristics and conversion efficiencies for the representative EDAS and ETAS-based BALs with cavity length of 4 mm are respectively plotted in Fig. 5(a) and (d), where the dashed lines are the idealized results neglecting LSHB and TPA effects, the dashed-dotted lines are the calculation results with only LSHB effect, and the solid lines are the results with both LSHB and TPA effects. The reduction in output power and conversion efficiency can be seen after LSHB and TPA effects are taken into account. The LSHB and the TPA power penalties (*i.e.*, the percentages of power reductions caused by the LSHB and the TPA effects respectively) for the two designs are also calculated in dependence on the injection current, as shown in Fig. 5(c) and (f). It can be seen that LSHB effect dominates the power penalty in the low bias regime. As discussed in previous references [17], [19], the magnitude of the LSHB penalty is directly correlated with the internal loss value. Since the internal loss of the EDAS/ETAS design is rather low, the performance degradation induced by the LSHB effect is not very serious. The calculated LSHB power penalties of the EDAS-based and ETAS based BALs are ~3.75% and ~2.5% respectively at the injection current of 30 A. The LSHB power penalty values remain relatively stable (the LSHB penalty of the EDAS design even decreases) with the increasing injection current. Conversely, the TPA power penalty grows with the injection current owing to the increasing photon density and outweighs the LSHB power penalty in the high injection regime. Although, as shown in Section III, the calculated values of direct modal TPA coefficient $\beta_{TPA}^{\text{direct,modal}}$ and indirect TPA absorption $\alpha_{TPA}^{\text{indirect,modal}}$ of the EDAS epitaxy ($t_n = 70$ nm) are much larger than those of the ETAS one with $t_n = 350$ nm, the narrower modal shape (narrower near field) and thus higher photon density in the ETAS-based BAL results in roughly the same TPA power penalties for both designs (*e.g.*, the calculated

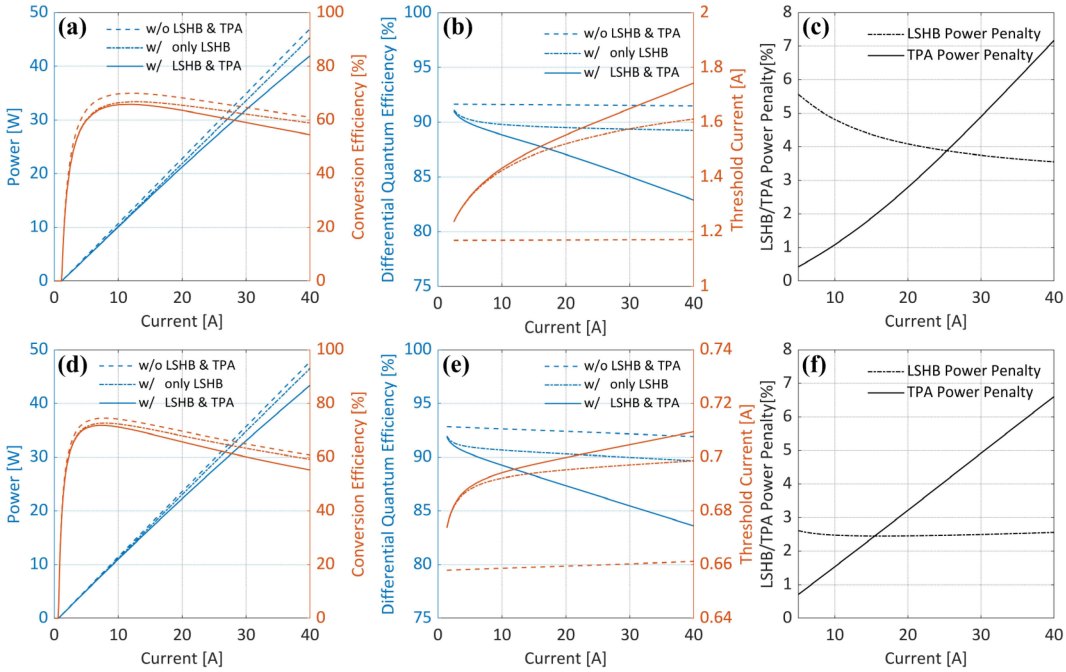

Fig. 5. Calculated L-I characteristics (Blue, left axis) and conversion efficiency (Red, right axis) for (a) the 4 mm-long EDAS-based BAL design with $t_n = t_p =$ 70 nm and (d) the 4 mm-long ETAS-based BAL design with $t_n = 350$ nm and $t_p = 70$ nm; DQE (Blue, left axis) and threshold current (Red, right axis) versus injection current for (b) the EDAS BAL and (e) the ETAS BAL; Calculated LSHB and TPA power penalty versus injection current for (c) the EDAS BAL and (f) the ETAS BAL. Here thermal effects are not considered.

TPA power penalties for the EDAS and ETAS designs at $I =$ 30 A are both around 4.9%). The current-dependent DQE and threshold current for the two devices are provided in Fig. 5(b) and (e) in order to better illustrate how the LSHB and TPA effects directly affect the laser output performance. As indicated by the figures, the LSHB effect accounts for most of the increase in the effective threshold current, whereas TPA just slightly increases the threshold current, indicating that the LSHB effect affects the non-stimulated recombination more than the TPA effect. Since the TPA effect affects the laser output power mainly via increasing the internal loss, that is, reducing the DQE, the drop in the DQE with the high injection current correlates to the increase in the TPA power penalty.

As for the EDAS design, the smaller confinement factor leads to a larger threshold current and thus a lower maximum conversion efficiency (∼5.5% lower than the ETAS one). On the other hand, the conversion efficiency of the ETAS design drops faster at high injection currents due to the large resistance and the serious TPA effect. To find the optimal values of structural parameters for the highest output power and efficiency, we sweep the *n*-confinement layer thickness t_n from 35 nm to 385 nm.The sweeping results for the output power and efficiency are plotted in Fig. 6(a) and (b), respectively. Clearly, the t_n value which leads to the maximum power and efficiency changes with the injection current. Fig. 6(c)–(e) respectively show the output power (upper panel) and the conversion efficiency (lower panel) as a function of t_n at three different currents $I =$ 20 A, 30 A and 36 A. Since the output power and efficiency values change slowly near the peak values, we define the 0.5% drop ranges of maximum output power and efficiency as the optimal t_n ranges, which are indicated as the translucent colored areas in Fig. 6(c)–(e). It can be seen that a large t_n value is in favor of high output power. As current grows and the TPA effect becomes more pronounced, the optimal t_n range shifts slightly to the smaller side. The optimal t_n ranges for the efficiency are lower than those for the output power. The overlaps of the translucent areas for the power and efficiency indicate the optimal ranges of the t_n parameter at the specific injection level. For $I =$ 20 A, 30 A, and 36 A, the optimal t_n range are centered at ∼325 nm, ∼255 nm, and ∼240 nm, respectively. Taken together, for 4 mm-length ETAS-based BAL under pulsed operating mode (i.e., no thermal effects) to achieve both high power and high efficiency in the current range of 20–36 A, the optimal range of t_n is about 250–300 nm.

The cavity length plays an important role in the performance of high-power diode laser. As discussed earlier, in the case of no LSHB and TPA effects, the threshold current generally increases and DQE decreases with the increase of cavity length. As a result, the achievable output power at a certain injection current decreases as the cavity length increases. Since LSHB and TPA effects are more serious as the cavity length increases, there is no doubt that under a certain injection current, the maximum output power will monotonically decrease with the cavity length, which is shown in the upper panels (left axis, hollow squares) of Fig. 7. To better illustrate the contribution of LSHB and TPA effects to the power reduction, Fig. 8 plots the LSHB and TPA power penalty at the maximum output power versus cavity length. For longer cavity length, the longitudinal spatial non-uniformity is more severe. It is evident from Fig. 8 that both LSHB and TPA power penalties at maximum output power monotonically increase with cavity length. Furthermore,

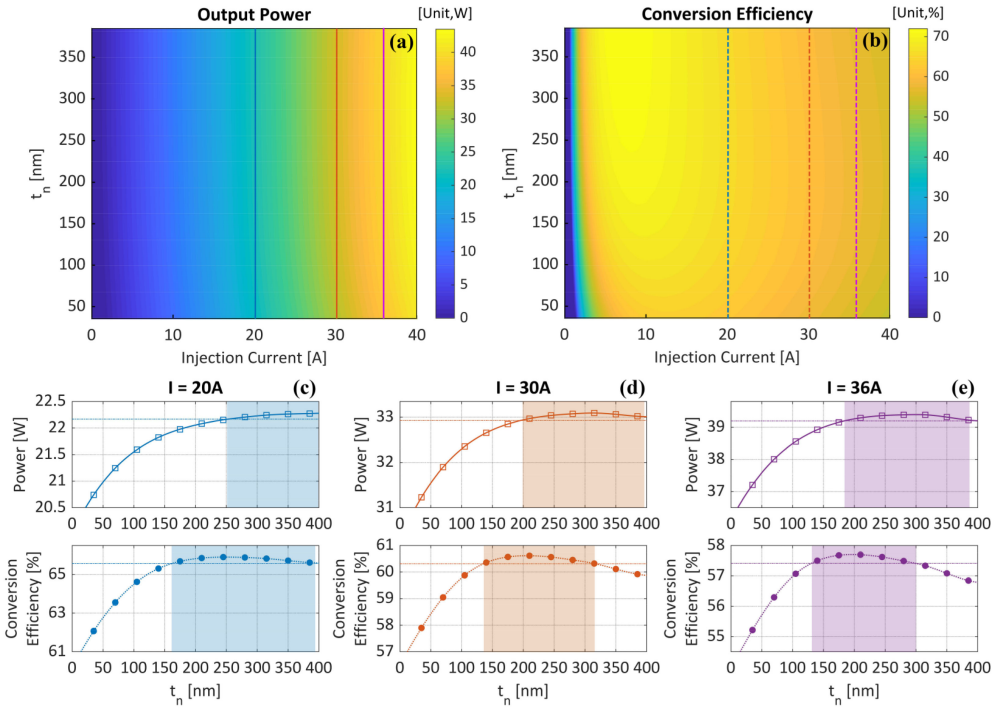

Fig. 6. The sweeping results for the output power (a) and conversion efficiency (b) of the 4 mm-long ETAS-based BAL as a function of the injection current I and n-confinement layer thickness t_n with both LSHB and TPA effects taken into account. (c)–(e) Output power (upper panel) and conversion efficiency (lower panel) as a function of t_n at various injection currents: (c) $I = 20$ A, (d) $I = 30$ A, and (e) $I = 36$ A. Thermal effects are not considered here. The rectangle and circle symbols are the calculation results, and the solid and dotted curves show the corresponding spherical linear interpolations.

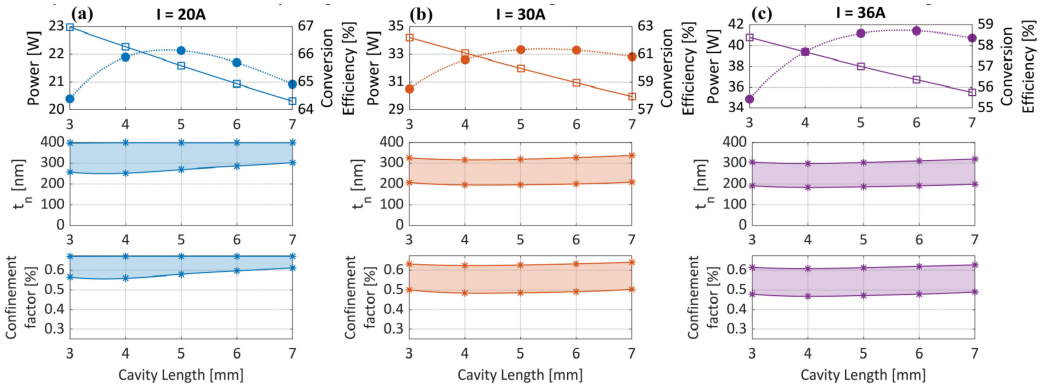

Fig. 7. Upper panels: the highest output power (left axis, hollow squares) and the highest conversion efficiency (right axis, filled circles) under different injection currents: (a) I = 20 A, (b) I = 30 A, and (c) I = 36 A. Middle/lower panels: the translucent areas show the overlap regions between the length-dependent optimal t_n/Γ ranges for power and efficiency under different injection currents. The symbols and curves respectively show the calculation results and the corresponding spherical linear interpolations. LSHB and TPA effects are included, while thermal effects are not considered here.

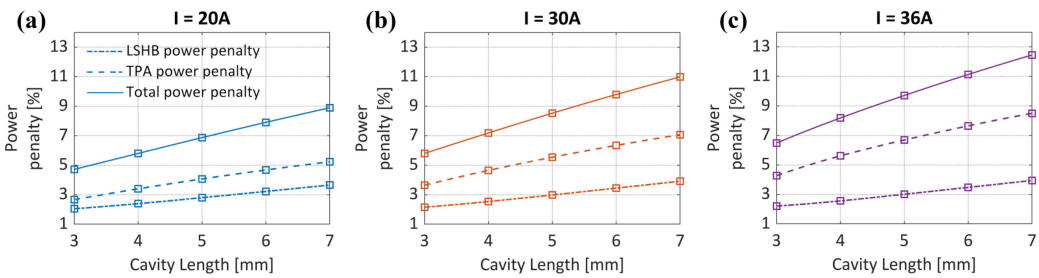

Fig. 8. Calculated LSHB and TPA power penalties of ETAS-based BALs at the maximum output power (corresponding to the hollow squares in the upper panels of Fig.7) versus cavity length under different injection currents: (a) I = 20 A, (b) I = 30 A, and (c) I = 36 A. (Thermal effects are not considered here).

the TPA power penalties under different cavity lengths are higher than the LSHB ones at these three injection currents, which is consistent with the previous discussion that the TPA effect dominates in the high injection regime.

On the other hand, longer cavity means lower device resistance, and thus higher conversion efficiency might be achieved. The conversion efficiencies of the ETAS-based BALs in dependence on the cavity length are also plotted in the upper panels (right axis, filled circles) of Fig. 7, which clearly illustrate the trade-off between the maximum achievable power and efficiency at a given injection level. At the three targeted injection currents $I = 20$ A, 30 A, and 36 A, the maximum efficiencies are found at cavity length of 5 mm, 5 mm, 6 mm, respectively. Moreover, with the increase of pumping level, the impact of cavity length on conversion efficiency becomes more obvious. At $I = 36$ A, the highest efficiency can reach 58.7% with a cavity length of 6 mm, whereas the highest efficiency is only 56.4% with a cavity length of 3 mm. The length-dependent optimal t_n overlap range for the power and efficiency are shown as the translucent colored areas in the middle panels of Fig. 7 and the corresponding optimal confinement factor overlap ranges are shown in the lower panels. As can be seen, the optimal t_n and confinement factor Γ range varies little with different cavity lengths at a specific injection current. The optimal t_n and Γ range tends to get smaller overall as the current increases to reduce the increasing negative effects of LSHB and TPA. To enable the ETAS-based BAL to have the most favorable performance under pulsed high-power operation for various cavity lengths from 3 mm to 7 mm and for a wide current range from 20 A to 36 A, the optimal choices of t_n and Γ are around 300 nm and 0.61%.

V. Design Optimization With Thermal Effects

As for a diode laser operating under CW mode, self-heating is another critical factor that limits its output power and efficiency. In this section, we will investigate the laser performance of EDAS/ETAS-based BALs with LSHB and TPA effects under CW operation. LASTIP is used here to better address the thermal effects of BALs with different design parameters. The BALs are assumed to be mounted p-side down onto CuW submounts. The heat sink is assumed to be kept at room temperature of 298K. In the LASTIP simulation, we apply the bottom n-type GaAs substrate with zero outgoing heat flux. For the top p-type contact, we assume it to be connected to a thermal conductor with a specified thermal conductance, the value of which is fitted from the experiment results in Refs [25], [26]. The extracted T_0 and T_1 characteristic temperatures of 4 mm length ETAS-based BALs are 183.5K and 572.8K for $t_n = 70$ nm, and 223.5K and 813.1K for $t_n = 350$ nm, respectively, which show good agreement with the experimental results reported in [24], [26] that the epitaxial structures with higher confinement factors show relatively higher T_0 and T_1 values. The effect of thermal lensing is considered in the LASTIP simulation by using 2.5e$-$4 K^{-1} as the temperature dependence of the thermal index change $\partial n/\partial T$ for AlGaAs [27]. To account for the thermal effects in the modified rate equation, we need to add the temperature and wavelength dependance to the material gain, that is, replace $g(N)$ with $g(N, T, \lambda)$, where T represents the temperature of the quantum well.

The calculated *L-I* and conversion efficiency curves of the representative 4 mm-long EDAS and ETAS-based BALs after considering the thermal effects are shown in Fig. 9(a) and (d). The corresponding current-dependent effective threshold current and DQE are also plotted in Fig. 9(b) and (e), serving as an alternative representation of *L-I* characteristics. Since the CW-driven diode lasers usually have the thermal roll-over and break down at a lower injection level than those under the pulsed mode, we reduce the studied current range to 0–30 A. It is worth pointing out that 30 A is still an ambitious operation point for a CW-driven BAL with 100um-wide stripe. According to state-of-the-art experiments, the sustainable range for CW operation is about 15–20 A. It can be clearly seen that the effective threshold currents of both designs, especially for the EDAS design with a small confinement factor, rise substantially with increasing bias current. This is because as the junction temperature increases with the bias current, the broadening of the Fermi distribution leads to a decrease in material gain [24]. To compensate the lower gain and the higher optical loss, the carrier density in the quantum well is increased (non-pinning) accordingly. This non-pinning effect of the carrier density results in increased carrier loss due to nonradiative recombination and carrier leakage, thereby leading to increased effective threshold current [24]. In addition, the increasing carrier density with temperature exacerbates the impact of LSHB. Fig. 9(c) and (f) respectively shows the calculated LSHB and TPA power penalty as a function of bias current for the two designs with thermal effects, which clearly show that the LSHB power penalty becomes larger than the case of no thermal effects. Moreover, the LSHB power penalty increases with bias in the high current region. TPA power penalties of both designs are basically the same as those in the case of no thermal effects. Accordingly, for the EDAS design with thermal effects, LSHB replaces TPA effect as the dominant effect in reducing output power within the targeted current range. The proportion of LSHB in the total power penalty of ETAS design is also considerably enhanced.

To find the optimal confinement factor at which the joint effect of LSHB and TPA on the device are minimum, n-confinement layer thickness t_n is swept from 35 nm to 385 nm, as illustrated in Fig. 10(a) and (b). To better illustrate the change trend of optimal t_n with the pumping level, Fig. 10(c)–(e) show the output power and conversion efficiency as a function of t_n at three different injection currents of $I = 15$ A, 20 A and 25 A. Here we also use the colored translucent areas to denote the 0.5% drop range of maximum output power and efficiency. Compared with the sweeping results in the absence of thermal effects shown in Fig. 6, it can be observed that the optimal t_n ranges for the output power and efficiency tend to overlap more in the presence of the thermal effects. For $I = 15$ A, 20 A, and 25 A, the optimal t_n overlap range are centered at $\sim$340 nm, $\sim$311 nm, and $\sim$280 nm, respectively. This result suggests that a relatively large t_n and confinement factor Γ should be adopted in the design of 4 mm-long ETAS-based BALs under the CW mode, which is consistent with the experimental results in [24] that a high-Γ ETAS design is beneficial for improving CW and short pulse performance at

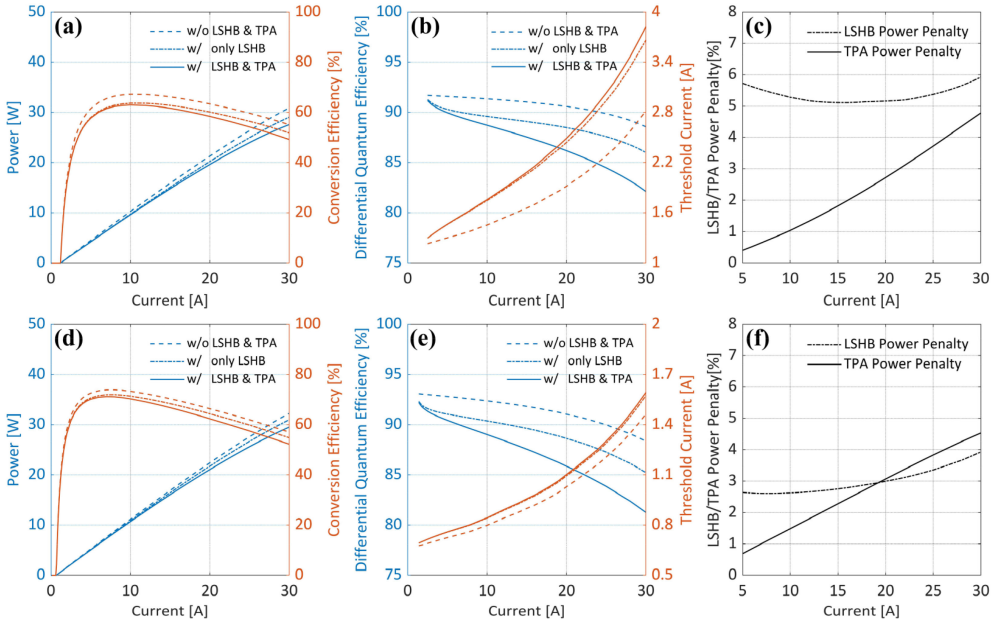

Fig. 9. Calculated L-I characteristics (Blue, left axis) and conversion efficiency (Red, right axis) for (a) the EDAS-based BAL design with $t_n = t_p = 70$ nm and (d) the ETAS-based BAL design with $t_n = 350$ nm and $t_p = 70$ nm; DQE (Blue, left axis) and threshold current (Red, right axis) versus injection current for (b) the EDAS BAL and (e) the ETAS BAL; Calculated LSHB and TPA power penalty versus injection current for (c) the EDAS BAL and (f) the ETAS BAL. Here thermal effects are included.

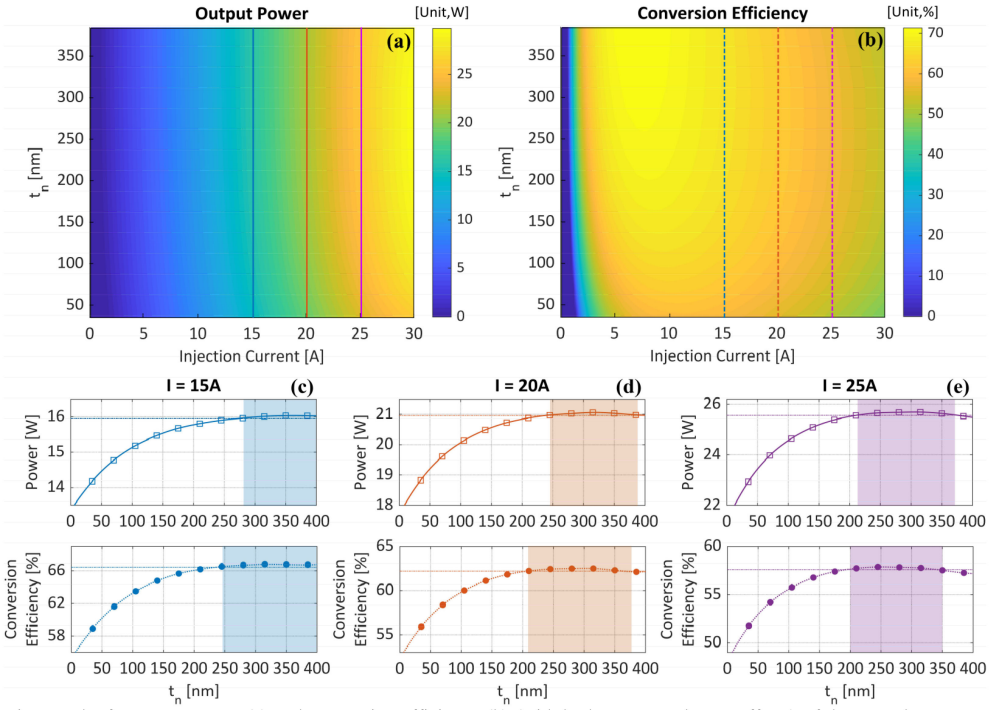

Fig. 10. The sweeping results for output power (a) and conversion efficiency (b) (with both LSHB and TPA effects) of the 4 mm-long ETAS-based BAL as a function of the injection current I and n-confinement layer thickness t_n after considering the thermal effects. (c)–(e) Output power (upper panel) and conversion efficiency (lower panel) as a function of t_n at various injection currents: (c) $I = 15$ A, (d) $I = 20$ A, and (e) $I = 25$ A.

high currents. As can be seen from Fig. 10, there is considerable overlap (280 nm–350 nm) between the optimal t_n ranges for the power and efficiency at these three different currents, indicating a large design margin in practice to achieve both high power and efficiency over a wide current range. Note that the power and efficiency drop rapidly as t_n approaches the lower sweeping limit of 35 nm. This is because the high nonradiative recombination in the low confinement factor design exacerbates the thermal effects, causing the rapid growth of effective threshold with the increase of the injection current.

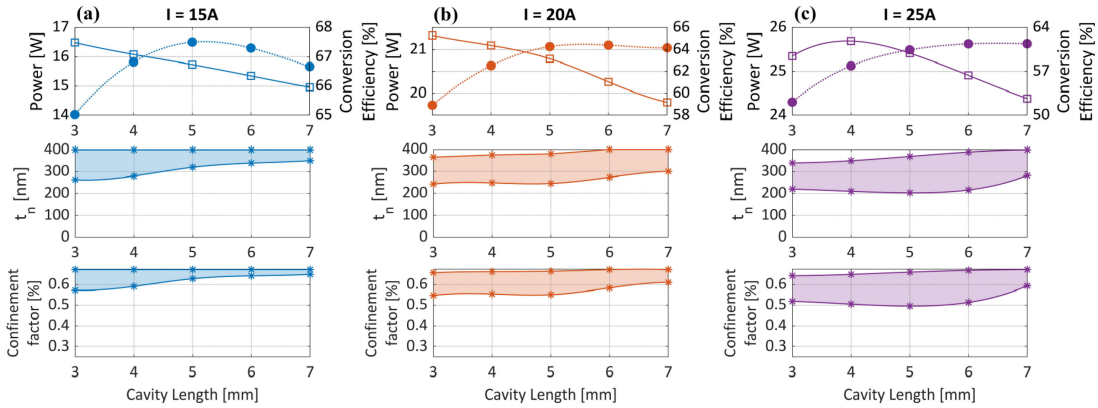

Fig. 11. Upper panels: the highest output power value (left axis, hollow squares) and the highest conversion efficiency value (right axis, filled circles) as a function of the cavity length under different injection currents (a) $I = 15$ A, (b) $I = 20$ A, and (c) $I = 25$ A; Middle/lower panels: the translucent areas show the overlap regions between the length-dependent optimal t_n/Γ ranges for power and efficiency under different injection currents. The symbols and curves respectively show the calculation results and the corresponding spherical linear interpolations. LSHB, TPA, and thermal effects are all included here.

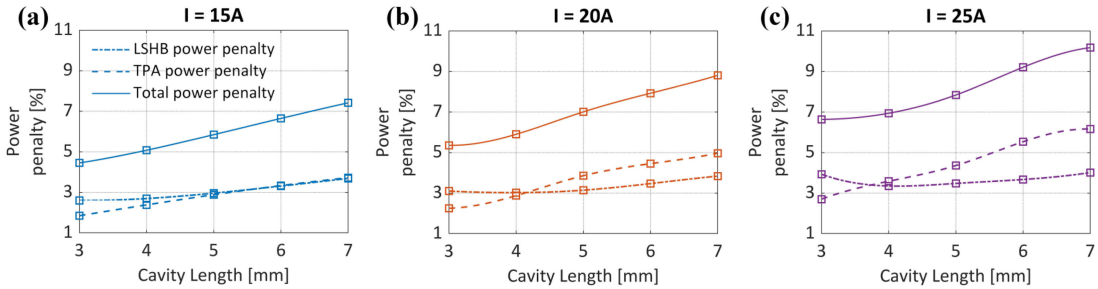

Fig. 12. Calculated LSHB and TPA power penalties of ETAS-based BALs at the maximum output power (corresponding to the hollow squares in the upper panels of Fig.11) versus cavity length under different injection currents: (a) I = 15 A, (b) I = 20 A, and (c) I = 25 A. (Thermal effects are considered here).

As mentioned earlier, the longer cavity length contributes to better thermal management owing to its lower thermal resistance. How to adjust the design parameters with different cavity lengths to achieve the best output performance of ETAS-based BALs under CW mode is studied. The calculated maximum output power and conversion efficiency of ETAS-based BAL as a function of cavity length under three different injection levels are plotted in the upper panels of Fig. 11. Fig. 12 shows the calculated LSHB and TPA power penalties a maximum output power versus cavity length. It can be noticed that the LSHB effect accounts for a larger fraction of the total power penalty for the shorter cavity length, where the thermal effects are more severe. The length-dependent optimal t_n and Γ overlap range for the power and efficiency areas are respectively shown in the middle and lower panels of Fig. 11, Evidently, longer cavity lengths do help increase the conversion efficiency, especially at the higher injection level (e.g., $I = 25$ A). For $I = 20$ A/25 A, the maximum efficiency is increased by 5.6%/9.3% by increasing the cavity length from 3 mm to 5.5/7 mm. Although at a certain bias current, a slight decrease in the output power with the increase of cavity length can be observed, their correlation becomes very weak at high injection levels. Hence, a relatively long cavity length (5–6 mm) is preferred for the ETAS-based BAL operating at high injection levels under the CW mode. As indicated by the middle and lower panels of Fig. 11, the optimal t_n and confinement factor Γ ranges tend to be a bit larger overall as the cavity length increases. Overall, the optimal t_n/Γ value for the CW driven ETAS-based BALs to maintain the optimum performance over a wide range of injection current and cavity length are around 345 nm/0.645%.

VI. Conclusion

Structural parameter optimization of EDAS/ETAS epitaxial designs for high-power and high-efficiency BALs is investigated by employing the modified rate equations with the LSHB and TPA effects taken into account. To better predict the performances of BALs based on different epitaxial structures, simulation software LASTIP is used to provide several key parameters that are required in rate equations, the TPA-generated free carrier densities for indirect TPA absorption calculation, the electric characteristics for conversion efficiency analysis, and thermal simulation under CW operation. The dependence of the two parameters describing the TPA effect in the modified rate equation—direct modal TPA coefficient βdirect,modal TPA and indirect TPA absorptions $\alpha_{TPA}^{\text{indirect,modal}}$—on the n-confinement layer thickness t_n are discussed. It is found that, in the case of pulsed mode operation, *i.e.*, in the absence of thermal effect, TPA effect acts as the dominant power saturation mechanism at high injection currents. As for the case of CW operation mode, the thermal effects exacerbate LSHB effect, and as a result, the proportion of LSHB power penalty to the total power penalty

significantly boosts. For both cases, with or without thermal effects, relatively large values of n-confinement layer thickness t_n and confinement factor Γ are beneficial to improve the output power and efficiency. Calculation results suggest that the optimal t_n/Γ value for the ETAS-based BAL design to maintain the optimal performance over a wide range of injection current and cavity length are $\sim$300 nm/0.61% for the pulsed mode and $\sim$345 nm/0.645% for the CW mode. It is noteworthy that the level of the confinement factor mentioned in this article is a relative term. The confinement factors of the ETAS structures are relatively low compared with a conventional symmetric waveguide epitaxial structure. Regarding the optimal choice of cavity length, there is a trade-off between the maximum achievable power and efficiency. The maximum output power generally decreases as the laser cavity increases, whereas the optimal cavity length for maximum conversion efficiency is around 5-6mm depending on the injection level for both cases of with or without thermal effects. For the case of CW mode, the increase in cavity length only results in a slow decrease in maximum output power but greatly improves the conversion efficiency. For example, by choosing the optimal cavity length, conversion efficiency improvements of 5.6% and 9.3% can be achieved at $I = 20$ A and 25 A, respectively. It should be pointed out that the mirror reflectance will also affect the optimization results, as the LSHB effect strongly depends on the difference between the mirror reflectances at the front and rear facets. The more unbalanced the mirror reflectance of the front and rear facets is, the more severe the LSHB effect is. However, the mirror reflectance optimization procedure is beyond the scope of this article. Our work is important for realizing high-power and high-efficiency BALs based on the EDAS/ETAS epitaxial structure as well as provides valuable guidelines for ongoing experimental implementation.

ACKNOWLEDGMENT

The authors wish to thank the anonymous reviewers for their valuable suggestions.

REFERENCES

[1] M. R. A.Hassan, F. Yu, W. J. Wadsworth, and J. C. Knight, "Cavity-based mid-IR fiber gas laser pumped by a diode laser," *Optica*, vol. 3, no. 3, pp. 218–221, 2016.

[2] H. Wenzel *et al.*, "High pulse power wavelength stabilized 905 nm laser bars for automotive LiDAR," in *Proc. IEEE High Power Diode Lasers Syst. Conf. (HPD)*, 2019, pp. 7–8.

[3] A. Pietrzak, M. Zorn, R. Huelsewede, J. Meusel, and J. Sebastian, "Development of highly efficient laser diodes emitting around 1060nm for medical and industrial applications," in *Proc. High-Power Diode Laser Technol. XVII*, 2019, vol. 10900, Art. no. 109000K.

[4] S. Schneider, I. Kardosh, M. Voß, S. Liebl, and J. Meinschien, "Power scaling of kW-diode lasers optimized for material processing applications," in *Proc. High-Power Diode Laser Technol. Appl. XIII*, 2015, vol. 9348, Art. no. 934808.

[5] P. Crump *et al.*, "Efficient high-power laser diodes," *IEEE J. Sel. Topics Quantum Electron.*, vol. 19, no. 4, Jul./Aug. 2013, Art. no. 1501211.

[6] K. H. Hasler *et al.*, "Comparative theoretical and experimental studies of two designs of high-power diode lasers," *Semicond. Sci. Technol.*, vol. 29, no. 4, 2014, Art. no. 045010.

[7] T. Kaul, G. Erbert, R. Platz, A. Maaßdorf, S. Knigge, and P. Crump, "Studies of limitations to peak power and efficiency in diode lasers using extreme-double-asymmetric vertical designs," in *Proc. Int. Semicond. Laser Conf.*, 2016, pp. 1–2.

[8] Y. Yamagata *et al.*, "915nm high-power broad area laser diodes with ultra-small optical confinement based on Asymmetric decoupled confinement heterostructure (ADCH)," in *Proc. High-Power Diode Laser Technol. Appl. XIII*, 2015, vol. 9348, Art. no. 93480F.

[9] T. Kaul, G. Erbert, A. Maaßdorf, D. Martin, and P. Crump, "Extreme triple asymmetric (ETAS) epitaxial designs for increased efficiency at high powers in 9xx-nm diode lasers," in *Proc. High-Power Diode Laser Technol. XVI*, 2018, vol. 10514, Art. no. 105140A.

[10] A. Boni, P. Della Casa, D. Martin, and P. Crump, "Efficiency optimization of high-power GaAs lasers by balancing confinement and threshold," in *Proc. 27th Int. Semicond. Laser Conf.*, 2021, pp. 1–2.

[11] A. Boni, S. Arslan, G. Erbert, P. Della Casa, D. Martin, and P. Crump, "Epitaxial design progress for high power, efficiency, and brightness in 970 nm broad area lasers," in *Proc. High-Power Diode Laser Technol. XIX*, 2021, vol. 11668, Art. no. 1166807.

[12] P. Crump *et al.*, "Increased conversion efficiency at 800 w continuous wave output from single 1-cm diode laser bars at 940 nm," in *Proc. Conf. Lasers Electro-Opt. Europe Eur. Quantum Electron.*, 2021, Paper cb_2_1. [Online]. Available: https://opg.optica.org/abstract.cfm?URI=CLEO_Europe-2021-cb_2_1

[13] F. Rinner, J. Rogg, P. Friedmann, M. Mikulla, G. Weimann, and R. Poprawe, "Longitudinal carrier density measurement of high power broad area laser diodes," *Appl. Phys. Lett.*, vol. 80, no. 1, pp. 19–21, 2002.

[14] H. Wenzel, P. Crump, A. Pietrzak, X. Wang, G. Erbert, and G. Tränkle, "Theoretical and experimental investigations of the limits to the maximum output power of laser diodes," *New J. Phys.*, vol. 12. no. 8, 2010, Art. no. 085007.

[15] Z. Chen *et al.*, "Performance limitation and mitigation of longitudinal spatial hole burning in high-power diode lasers," in *Proc. Novel -Plane Semicond. Lasers XI*, 2012, vol. 8277, Art. no. 82771J.

[16] J. Piprek and Z. M. Li, "What causes the pulse power saturation of GaAs-based broad-area lasers?," *IEEE Photon. Technol. Lett.*, vol. 30, no. 10, pp. 963–966, May 2018.

[17] E. A. Avrutin and B. S. Ryvkin, "Effect of spatial hole burning on output characteristics of high power edge emitting semiconductor lasers: A universal analytical estimate and numerical analysis," *J. Appl. Phys.*, vol. 125, no. 2, 2019, Art. no. 023108.

[18] M. Dogan, C. P. Michael, Y. Zheng, L. Zhu, and J. H. Jacob, "Two photon absorption in high power broad area laser diodes," in *Proc. High-Power Diode Laser Technol. Appl. XII*, 2014, vol. 8965, Art. no. 89650P.

[19] A. Demir, M. Peters, R. Duesterberg, V. Rossin, and E. Zucker, "Semiconductor laser power enhancement by control of gain and power profiles," *IEEE Photon. Technol. Lett.*, vol. 27, no. 20, pp. 2178–2181, Oct. 2015.

[20] E. A. Avrutin and B. S. Ryvkin, "Theory of direct and indirect effect of two-photon absorption on nonlinear optical losses in high power semiconductor lasers," *Semicond. Sci. Technol.*, vol. 32, no. 1, 2016, Art. no. 015004.

[21] "Crosslight device simulation software-general manual," Crosslight Software Inc., Vancouver, BC, Canada, 2020, p. 1164.

[22] L. A. Coldren, S. W. Corzine, and M. L. Mashanovitch, *Diode Lasers and Photonic Integrated Circuits*. New York, NY, USA: Wiley, 2012.

[23] I. P. Marko, A. R. Adams, N. F. Massé, and S. J. Sweeney, "Effect of non-pinned carrier density above threshold in InAs quantum dot and quantum dash lasers," *IET Optoelectron.*, vol. 8, no. 2, pp. 88–93, 2014.

[24] T. Kaul, G. Erbert, A. Klehr, A. Maaßdorf, D. Martin, and P. Crump, "Impact of carrier nonpinning effect on thermal power saturation in GaAs-Based high power diode lasers," *IEEE J. Sel. Topics Quantum Electron.*, vol. 25, no. 6, pp. 1–10, Nov./Dec. 2019.

[25] S. Arslan *et al.*, "Approaches for higher power in GaAs-based broad area diode lasers," in *Proc. IEEE High Power Diode Lasers Syst. Conf.*, 2019, pp. 51–52.

[26] T. Kaul, G. Erbert, A. Maaßdorf, S. Knigge, and P. Crump, "Suppressed power saturation due to optimized optical confinement in 9xx nm high-power diode lasers that use extreme double asymmetric vertical designs," *Semicond. Sci. Technol.*, vol. 33, no. 3, 2018, Art. no. 035005.

[27] H. Wenzel, M. Dallmer, and G. Erbert, "Thermal lensing in high-power ridge-waveguide lasers," *Opt. Quantum Electron.*, vol. 40, no. 5, pp. 379–384, 2008.